THE JOURNAL OF
PHYSICAL CHEMISTRY C

Article

pubs.acs.org/JPCC

Ambipolar Behaviors of Hydrogen-Incorporated ZnO Nanowires

Abhishek Prasad,[†] Archana Pandey,[†] Vamsi Krishna Kunapuli,[‡] Paul L. Bergstrom,[‡] and Yoke Khin Yap*,[†]

[†]Department of Physics and [‡]Department of Electrical and Computer Engineering, Michigan Technological University, Houghton, Michigan 49931, United States

S *Supporting Information*

ABSTRACT: Ambipolar behaviors of zinc oxide nanowires (ZnO NWs) are obtained for the first time by controlled annealing in hydrogen ambient. Optimum annealing can create *p*-type acceptors into ZnO NWs while maintaining the *n*-type donors from the as-grown samples. We found that such optimum condition must be one that is more than sufficient to eliminate the green photoluminescence (PL) band of the as-grown ZnO NWs. All of these can be explained by an ab initio model of Zn vacancy-hydrogen complexes, which can served as the donor, acceptor, or green PL quencher depending on the number of hydrogen atoms involved.

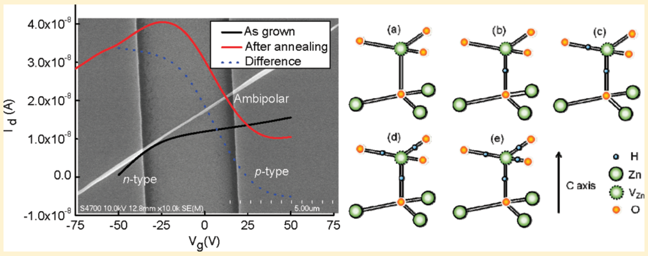

INTRODUCTION

Unintentional *n*-type conductivity observed in as-grown zinc oxide (ZnO) has been a major issue for achieving high-performance electronic, optical, and sensing devices.[1] These *n*-type behaviors have been attributed to native point defects such as oxygen and zinc vacancies. However, recent theoretical study shows that this might not be true.[2] Theory suggests that oxygen vacancies are deep donors with high formation energies in ZnO. Besides, zinc vacancies are deep acceptors and act as compensating centers in *n*-type ZnO. Defects due to the presence of donor impurities such as hydrogen-related complex are being studied as a possible reason for unintentional *n*-type behavior in as-grown ZnO.[3] In addition, native defect complex with nitrogen was also been found to contribute to *n*-type conductivity in ZnO.[4] Apparently, defects and their complexes play even more important roles in electrical properties of ZnO nanostructures due to the larger unsaturated bonds on their surfaces.

There are some efforts in reducing the contribution of defects on electrical properties of ZnO nanostructures. These can be classified into two general approaches: (1) postsynthesis coating of ZnO NWs with other materials and (2) annealing of the as-grown ZnO NWs in various gases. Song et al.[5] show that coating of poly(methyl methacrylate) (PMMA) layer could passivate the environment effect on the behaviors of ZnONW field effect transistors (FETs). Similarly Chang et al.[6] reported on passivation of ZnONW FETs using SiO_2/Si_3N_4 bilayer. Passivation by SiO_2/Si_3N_4 bilayer significantly enhances device characteristics such as mobility, subthreshold swing, on/off ratio, and so on. In a similar attempt, Park et al.[7] passivated ZnO nanorod FETs with polyimide thin layer and obtained a significantly improved on−off ratio and higher mobility. Recently, Jhu et al.[8] enhanced the performance of ZnONW FETs by annealing in Ozone. In another approach Keem et al.[9] remarkably enhanced the performance of ZnONW FETs by annealing in hydrogen gas at 350 °C. Unfortunately, in all of these passivation and annealing approaches, ZnO NWs retained their *n*-type behaviors. In fact, there are only a few successes in creating *p*-type carriers in ZnO NWs by doping with the use of additional P_2O_5,[10] N_2O,[11] or Zn_3P_2[12] in the starting materials.

Here we show that controlled incorporation of hydrogen into ZnO NWs can introduce *p*-type characters to the nanowires. We further found that the *n*-type behaviors remained, leading to the ambipolar behaviors of hydrogen incorporated ZnO NWs. Importantly, the detected *p*- and *n*-type behaviors are stable for longer than 2 years when devices were kept under ambient conditions. It is noted that ambipolar behaviors have recently gained attention for the ability to control device polarity (*p*- or *n*-type) by a gate electrode and open up new opportunity in creating novel analog and digital devices.[13,14] In our approach, FETs were first fabricated by as-grown ZnO NWs. Part of the as-grown sample was subjected to a series of systematic annealing processes in hydrogen ambient at a temperature range beyond what have been reported. More FETs were fabricated from these annealed samples for comparison. Our approach is thus different from previously demonstrated annealing efforts. In all reported annealing approaches, the whole ZnONW FETs were subjected to the annealing process.[9] This has limited the annealing condition at low temperatures. In addition, the electrodes and the contact resistance of the devices are subjected to change during annealing, and thus the true nature of enhancement due to ZnO NWs cannot be fully ascertained. All of these issues were eliminated in our approach. We found that *p*-type behaviors were introduced only at a well-defined window of annealing temperature, duration, and gas flow rate.

Received: January 10, 2012
Revised: March 14, 2012
Published: March 14, 2012

dx.doi.org/10.1021/jp3003118 | *J. Phys. Chem. C* 2012, 116, 8210−8215

■ EXPERIMENTAL DETAILS

Our ZnO NWs are grown in a double quartz tube configuration thermal chemical vapor deposition (CVD), as previously described.[15] In short, the growth of ZnO NWs was performed in a horizontal furnace consisting of a quartz tube vacuum chamber. A smaller quartz tube (60 cm long and 2 cm in diameter) containing the precursor materials and the substrates were placed within the vacuum chamber. A mixture of ZnO (0.2 g) and graphite (0.1 g) powder in an alumina boat was used as the precursor materials. These are placed at the closed end of the smaller quartz tube. A series of bare silicon substrates was then placed downstream from the mixture in the small quartz tube. The small tube was then inserted into the vacuum chamber such that the closed end is at the center of the furnace. The temperature of the furnace was raised to 1100 °C. At ~350 °C, oxygen gas was introduced into the furnace at a flow rate of 10 sccm. The temperature was held at 1100 °C for 30 min and turned off to allow cooling to 600−700 °C in ~1 h. Experiment was stopped by opening the heating panel of the furnace and allowing the system to cool to room temperature. The as-grown ZnO NWs sample was examined with scanning electron microscopy (SEM) using Hitachi S-4700 FE-SEM. Photoluminescence (PL) spectroscopy is also performed using a HeCd laser (excitation wavelength ~325 nm) in a Jobin-Yvon LabRAM HR800 spectrometer. Raman spectroscopy is also performed using Jobin-Yvon LabRAM HR800 spectrometer. These ZnO NWs were then subjected for annealing. All sample, before and after annealing, were examined with SEM, PL, and Raman spectroscopy.

Backgate FETs are fabricated using standard photolithography techniques. As-grown or annealed ZnO NWs are suspended in ethanol by ultrasonic bath of the sample for a few minutes. Droplets of this suspension are then coated on clean oxidized Si substrates (500 nm SiO_2). Arrays of electrode pad (Nickel films with thickness of 250 nm) are then coated using magnetic sputtering. All FETs are then characterized by using a Keithley 4200 semiconductor characterization system. All FETs characterized here consist of one ZnO NWs across the source (S) and drain (D) electrodes, as shown in Figure S1 (Supporting Information).

■ RESULTS

As-grown ZnO NWs were annealed at 700 °C (hydrogen flow rate = 40 sccm, duration = 30 min). Figure 1 shows PL spectra before and after annealing. Typical PL spectra for ZnO NWs have a predominant peak at ~380 nm with intensity I_{uv} and I_{uv}' for the as-grown and annealed samples, respectively. These peaks are corresponding to the near-band-edge emission of ZnO attributed to the recombination of the free excitons.[15] In addition, PL peaks at ~520 nm are also observed with intensity I_{green} and I_{green}' for the as-grown and annealed samples, respectively. These green peaks are recently attributed to intraband defect level due to zinc vacancies.[2,16] Previously this was assigned to singly ionized oxygen vacancies in ZnO.[17] As shown in Figure 1, the intensity of the defect-related peak has reduced after annealing ($I_{green}' < I_{green}$). The intensity peak ratio, I_{uv}/I_{green} is ~1.21 and the peak ratio after annealing (I_{uv}'/I_{green}') is ~1.58, indicating a decrease in defect level. The broad defective peak is due to the contribution of various defect-related components and can be deconvoluted to multiple Gaussian bands.[18] A slight shift between the peaks of I_{green} and I_{green}' is observed here and may be due to the change in degree of contribution of these components.

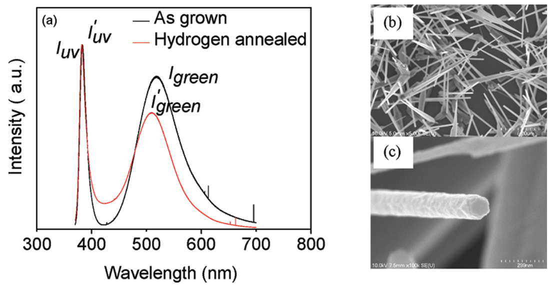

Figure 1. (a) PL spectra of ZnO NWs before and after annealing at 700 °C (hydrogen flow rate = 40 sccm, duration = 30 min). SEM images of the as-grown (b) and annealed (c) NWs.

The reduction of the defect-related peak demonstrated here is encouraging. However, SEM image after annealing revealed that the surface of the nanowires became rough (Figure 1c). We think that in addition to defect passivation the high annealing temperature and high hydrogen flow rate employed here have led to chemical etching of the nanowire surface. This can be explained by the fact that hydrogen may have reduced the surface of ZnO NWs to Zn,[17,19] followed by melting of Zn (melting point = 420 °C) and making the rough surface morphology. We also found that annealing performed at higher temperatures (for example at 900 °C) increased the defect band peak, as shown in the Supporting Information (Figure S2).

We have thus reduced the annealing temperatures, the hydrogen flow rates, and the annealing duration. After a series of experiments, we have identified a promising window where optimum annealing can be obtained, which could suppress the defective PL peak at ~520 nm without deteriorating the surface of ZnO NWs. For example, PL spectra and SEM images of ZnO NWs before and after annealing at 600 °C (hydrogen flow rate = 10 sccm, duration = 15 min) are shown in Figure 2. As shown, the defect-related peak at ~520 nm is not detectable. PL signals due to real electron transitions will lead to Gaussian-like features. Here the PL spectra is flat in the range of 450−600 nm. This means that no obvious luminescence occurred due to the present of defective bands. It is also noted that a higher baseline is observed near the range of longer wavelengths, which is quite common in our as-measured spectra. (See, for example, Figures S4 (b), S5 (a), S6 (b), and S7 (a) in the Supporting Information, which have obvious defective peaks.) As shown in various PL spectra in the Supporting Information, the change of the baseline level in these as-measured spectra can occur at wavelengths near ~700

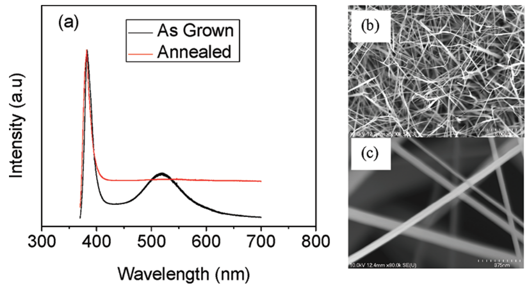

Figure 2. (a) PL spectra of ZnO NWs before and after annealing at 600 °C (hydrogen flow rate = 10 sccm, duration = 15 min). SEM images of the as-grown (b) and annealed (c) ZnO NWs.

or ~370 nm. We think that these are due to the change of sensitivity of the CCD detector during measurement at room temperatures. From high-resolution SEM, the surface morphology of ZnO NWs after annealing is smooth. This means that the surfaces of ZnO are not reduced by hydrogen into Zn under this milder annealing condition and prevented surface melting and roughening. This result showed that the annealing condition applied here is optimum to reduce the defects in ZnO NWs. In fact, annealing at slightly lower temperatures (for example, at 500 °C) can also reduce the defect-related PL peak (Figure S3 in the Supporting Information) but not optimum. More examples for annealing conducted at 600 °C at various hydrogen flow rates and annealing durations are shown in the Supporting Information (Figures S4−S8).

Raman spectra for as-grown and optimally annealed ZnO NWs are obtained by using a HeNe laser (wavelength = 632.8 nm). As shown in Figure 3, the as-grown sample-initiated scattering at Raman shifts of 304 (due to the Si substrate), 334 ($E_{2H\text{-}2L}$ mode of ZnO NWs), 377 (A_{1T} mode of ZnO NWs), 438 (E_{2H} mode of ZnO NWs), 520 (due to the Si substrate), and 618 cm^{-1} (due to the Si substrate). These modes compare well with the ZnO phonon modes for bulk ZnO and ZnO NWs in literature.[20−22] Similarly, Raman spectra were obtained from the hydrogen annealed sample with phonon frequencies at 304, 334, 377, 438, 520, and 618 cm^{-1} without obvious changes in intensity as that reported for ZnO powders.[20] These Raman spectra suggest that ZnO NWs maintain their crystalline structure after annealing and our annealing condition is optimum

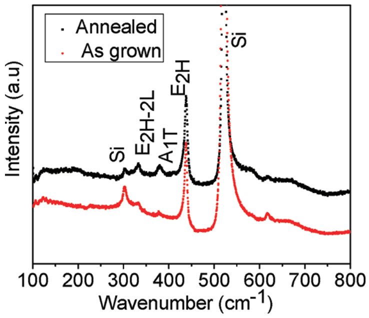

Figure 3. Raman spectra of ZnO NWs before and after annealing at 600 °C (hydrogen flow rate = 10 sccm, duration = 15 min).

The electronic transport properties of FETs fabricated by using as-grown and optimally annealed ZnO NWs are then characterized. Each FET has an individual ZnO NW connected across the source and drain electrodes. The PL spectra of these NWs were reconfirmed by mapping under a confocal microscope. As shown in Figure 4a, FETs fabricated by as-grown NWs have a strong defect-related luminescence band, as detected at the wavelength window of 450−600 nm (graphically labeled as green). This is not detected in FETs fabricated by optimally annealed NWs. As shown in Figure 4b, only the strong near band edge emission (graphically labeled as red) was detected at the window of 350−390 nm.

For FETs fabricated by as-grown ZnO NWs, the typical behaviors of drain current (I_d) as a function of drain voltage (V_d) at different gate voltages (V_g) are summarized in Figure 5a. As shown, I_d initially increases almost linearly with V_d and starts to saturate at ~2 to 3 nA when $V_d > 3$ V. This is a typical I_d−V_d behavior for n-type semiconductors with electrons as the charge carriers, and channel pinch-off starts to occur near the drain electrode at $V_d > 3$ V. The channel resistance at $V_g = 0$ V is estimated from the near-linear region as $R \approx 1.5\ \Omega$. At higher V_d, I_d is weakly dependent on V_d but can be increase by V_g, indicating the n-type behaviors of the as-grown NWs. The transconductance for this FET is obtained from slope of linear region of the I_d−V_g curves at different V_d, as shown in Figure 5b. The slope at these linear regions can be represented by[23]

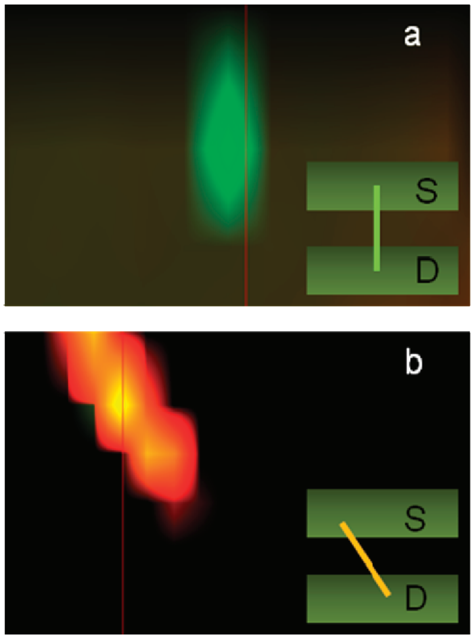

Figure 4. Typical PL maps of individual ZnO NWs connected across source (S) and drain (D) electrodes (schematic in the insets). (a) An as-grown NW with strong luminescence at 450−600 nm. (b) An optimally annealed NW with strong luminescence at 350−390 nm.

$$\frac{\mathrm{d}I_\mathrm{d}}{\mathrm{d}V_\mathrm{G}} = \frac{\mu C}{L^2} V_\mathrm{d} \tag{1}$$

where μ is carrier mobility, L is the length of the nanowire channel (4 μm in this case), and C is the capacitance of the channel. For nanowire FET with cylindrical geometry, capacitance is given by[23]

$$C = \frac{2\pi L \varepsilon_{\mathrm{SiO}_2} \varepsilon_0}{\ln\left(\frac{4h}{d}\right)} \tag{2}$$

where h (500 nm) is the thickness of gate SiO_2, d is nanowire diameter (80 nm), and $\varepsilon_{\mathrm{SiO}_2}$ (=3.31) is the dielectric constant of SiO_2. For the FET constructed by as-grown ZnO NWs, the carrier mobility (μ) is 0.0066 $\mathrm{cm}^2\ \mathrm{V}^{-1}\ \mathrm{s}^{-1}$ at $V_d = 20$ V. This value is lower than some reported values[23,24] because of the back gate configuration we employed with a thick oxide layer (500 nm).

For FETs fabricated by ZnO NWs annealed under our optimum condition, the behaviors of drain current (I_d) as a function of drain voltage (V_d) at different gate voltages (V_g) are summarized in Figure 6a. As shown, I_d increases almost linearly with V_d and starts to saturate at ~25−30 nA when $V_d > 15$ V. As shown, current saturation occurred at much higher I_d and V_d values compared with the case of FETs fabricated by as-grown NWs. The channel resistance at $V_g = 0$ V is estimated from the near-linear region as $R \approx 0.3\ \Omega$, much lower than that of as-

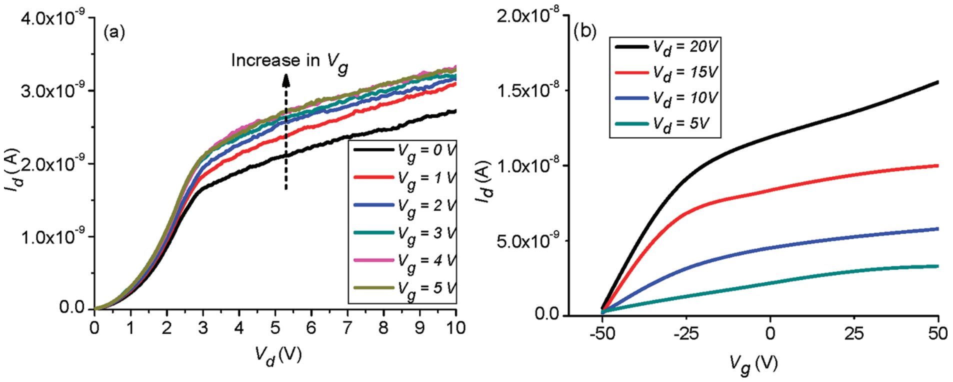

Figure 5. Typical (a) I_d−V_d curves for FETs fabricated by as-grown ZnO NWs with V_g vary from 0 to 5 V. (b) Related I_d−V_g curves with V_d vary from 5 to 20 V.

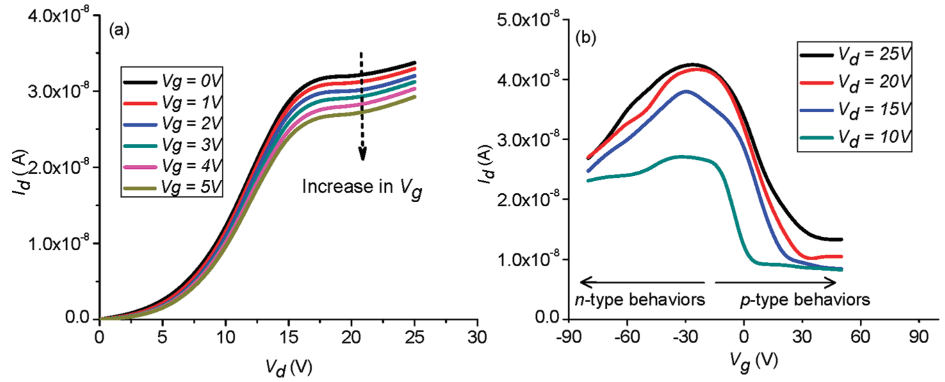

Figure 6. Typical (a) I_d−V_d curves for FETs fabricated by annealed ZnO NWs with V_g varies from 0 to 5 V. (b) Related I_d−V_g curves with V_d vary from 10 to 25 V.

grown NWs. Furthermore, we found that I_d decreases with the increase in V_g at V_d > 15 V, a reverse trend as compared with Figure 6a. This is the typical gating behavior for *p*-type FETs. To analyze further the behaviors of this FET, the I_d−V_g curves at different V_d are plotted in Figure 6b. As V_g increases from −80 to ∼ −20 V, I_d of the NW channel increases accordingly. This is the typical behavior for *n*-type channels, and thus the detected I_d is electron current. However, further increase in V_g leads to the decrease in I_d, which is the behavior for *p*-type channels and thus the detected I_d is hole current. This means, the I_d−V_g curves at different V_d in Figure 6b indicate that annealed ZnO NWs are ambipolar, having both *n*-type and *p*-type behaviors. These ambipolar behaviors are very reproducible, as shown in a series of I_d−V_g curves for different FETs fabricated by different patches of annealed ZnO NWs (Figure S9 in the Supporting Information).

To demonstrate further the ambipolar behaviors of our annealed ZnO NWs, we have, for example, extracted the I_d−V_g curves at V_d = 20 V from Figures 5b and 6b and placed them together in Figure 7. As shown, the I_d−V_g curve for FETs fabricated by as-grown NWs (black curve, *n*-type) behaves significantly different than the I_d−V_g curve for FETs fabricated by annealed NW (red curve, ambipolar). We have then numerically extracted the difference between these two curves and plotted the resultant curve in blue. As shown, the resultant curve behaves as a typical *p*-type FETs, a reverse trend as the black curve (*n*-type). This numerical extraction clearly indicates that the annealed NWs contained both *p*- and *n*- carriers and resembled characters of an ambipolar channel, and the associated *p*-type behavior can be qualitatively extracted after subtracting *n*-type behavior in the as-grown NWs. The carrier mobility (μ) as estimated from the slope at the linear region of the resultant curve is 0.0288 cm^2 V^{-1} s^{-1}, four-fold higher than the case for as-grown NWs. It is noted that this analysis is just qualitatively correct but may not be quantitatively accurate because the I_d versus V_g data are produced by different FETs. However, because these FETs are fabricated using nanowires grown on the same samples (with and without hydrogen annealing), we think that such an analysis is qualitatively meaningful.

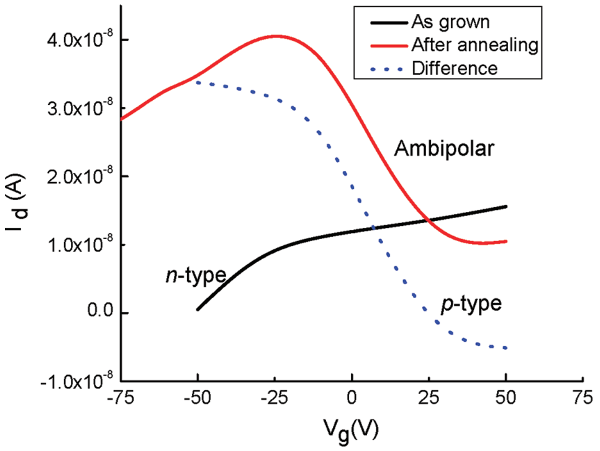

Figure 7. I_d−V_g curves at V_d = 20 V for FETs fabricated by as-grown (black curve) and annealed (red curve) ZnO NWs. The difference between these curves is plotted in a blue curve.

DISCUSSION

In short, hydrogen annealing contributed to two major effects: (1) quenching of the green PL peaks and (2) creation of the *p*-type carriers. The possible mechanism involved is discussed here. In our case, the growth of ZnO NWs takes place under oxygen-rich conditions because oxygen gas is continuously flown. This will likely lead to the formation of zinc vacancies (V_{Zn})[2,16] that contribute to the defective green PL band.[25,26] However, V_{Zn} is a deep acceptor in ZnO[25,27] and will not contribute to *p*-type behavior. Our result suggests that hydrogen annealing quenches these defects, as observed by the absence of the defect PL band in annealed ZnO NWs. In fact, hydrogen atom interacts with V_{Zn} to form various types of V_{Zn}-hydrogen complexes.[28,29] In particular, the formation of V_{Zn}-H_2 complex has been identified for the quenching of green luminescence,[29,30] and the phenomenon was experimentally observed.[29−32] We thus believed that one of the functions of hydrogen annealing in our case is the passivation of zinc vacancies by forming V_{Zn}-hydrogen complexes. The mechanism of creating *p*-type and *n*-type carriers is discussed hereafter based on a model developed by ab initio calculation.[28]

Depending on the number of hydrogen atoms at the site of zinc vacancy, the possible bonding structure of the V_{Zn}-hydrogen complexes is different, as shown in Figure 8. The schematic of V_{Zn} without any H is a double acceptor and is shown in Figure 8a. This is a deep acceptor that initiates the defect PL peak in as-grown ZnO NWs and will not contribute to *p*-type behavior. The first possible complex has one H, as shown in Figure 8b, and is denoted as 1(O−H)-V_{Zn} complex. This complex is a single acceptor because one of the missing charges in V_{Zn} is now compensated. Figure 8c−e are denoted as 2(O−H)-V_{Zn}, 3(O−H)-V_{Zn}, and 4(O−H)-V_{Zn}, complexes, respectively. Clearly, two H atoms in 2(O−H)-V_{Zn} will compensate the missing charges created by V_{Zn} and do not contribute free carrier. Therefore, the formation of 2(O−H)-V_{Zn} complex will not create any doping level within the band gap of ZnO and lead to the quenching of green PL peak.3(O−H)-V_{Zn} and 4(O−H)-V_{Zn} will contribute one and two additional electrons, respectively, and create donor levels in ZnO. Hence 1(O−H)-V_{Zn} complex is the only possible structure in our annealed ZnO NWs, which contributed to the *p*-type carriers, whereas3(O−H)-V_{Zn} and 4(O−H)-V_{Zn} could act as the donors. Coexistence of these acceptors and donors is the likely reason for the ambipolar behaviors in our FETs.

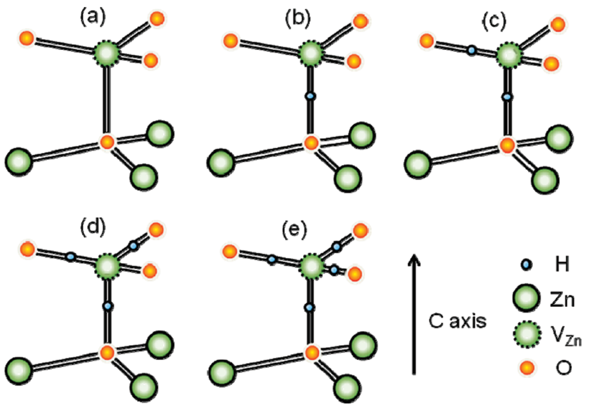

Figure 8. Schematic of V_{Zn}−hydrogen complexes in ZnO lattice[25] (a) without vacancy and hydrogen, (b) 1(O−H)-V_{Zn}, (c) 2(O−H)-V_{Zn}, (d) 3(O−H)-V_{Zn}, and (e) 4(O−H)-V_{Zn}.

CONCLUSIONS

To summarize our discussion, we interpret our results based on the scenario of V_{Zn}-hydrogen complexes. We think that both V_{Zn} and 4(O−H)-V_{Zn} are presented in as-grown ZnO NWs, which is responsible for the green PL band and the *n*-type behaviors, respectively. The present of V_{Zn} in as-grown ZnO NWs is well-accepted.[2,16,26,27] The 4(O−H)-V_{Zn} is most energetically stable among all V_{Zn}-hydrogen complexes,[28] which could have been formed due to the present of trace water vapors in the growth chamber and starting materials (ZnO and graphite powders, quartz chamber, Si substrates, etc.). Of course, we did ignore the present of 3(O−H)-V_{Zn} complexes because their formation energy is just slightly higher than that of 4(O−H)-V_{Zn} complexes.[28] The possible reason for the reported enhanced performance of FETs[9] after annealing the devices in hydrogen ambient at 350 °C could be the formation of more 3(O−H)-V_{Zn} and 4(O−H)-V_{Zn} complexes. However, the annealing temperature could be too low to overcome the needed formation energy for the creation of 1(O−H)-V_{Zn} complexes, which is the highest among all known complexes shown in Figure 8. Under our optimum annealing condition at ~600 °C, both 1(O−H)-V_{Zn} and 2(O−H)-V_{Zn} complexes are formed, leading to the *p*-type behavior and quenching of the green PL band, respectively. Because the formation energy of 2(O−H)-V_{Zn} complexes is just slightly lower than that of 1(O−H)-V_{Zn},[28] the optimum annealing condition for the formation of *p*-type carriers, the 1(O−H)-V_{Zn} complexes, must be one that is more than sufficient to suppress the green PL band.

ASSOCIATED CONTENT

Ⓢ Supporting Information

SEM of a typical FET. PL spectra of ZnO NWs before and after annealing under various conditions. Ambipolar behaviors of various FETs. This material is available free of charge via the Internet at http://pubs.acs.org.

AUTHOR INFORMATION

Corresponding Author

*E-mail: ykyap@mtu.edu.

Notes

The authors declare no competing financial interest.

ACKNOWLEDGMENTS

This work is currently supported by the National Science Foundation (award no. 0926819, Civil, Mechanical and Manufacturing Innovation Division) and Michigan Tech Multi-Scale Technologies Institute (*MuSTI*). The initial phase of this work was supported by the Defense Advanced Research Projects Agency (contract number DAAD17-03-C-0115 through the U.S. Army Research Laboratory).

REFERENCES

(1) (a) Yan, R.; Gargas, D.; Yang, P. *Nat. Photonics* **2009**, *3*, 569. (b) Fan, Z.; Lu, J. G. *J. Nanosci. Nanotechnol.* **2005**, *5*, 1561. (c) Prasad, A.; Mensah, S.; Pan, Z. W.; Yap, Y. K. Chapter 4. In *Sensors Based on Nanostructured Materials*; Arregui, F. J., Ed.; Springer: New York, 2009, pp 59−78.

(2) Janotti, A.; Van de Walle, C. G. *Phy. Rev. B* **2007**, *76*, 165202.

(3) McCluskey, M. D.; Jokela, S. J. *Physica B* **2007**, *401−402*, 355.

(4) Look, D. C.; Farlow, G. C.; Reunchan, P.; Limpijumnong, S.; Zhang, S. B.; Norlund, K. *Phys. Rev. Lett.* **2005**, *95*, 225502.

(5) Song, S.; Hong, W. K.; Kwon, S. S.; Lee, T. *Appl. Phys. Lett.* **2008**, *92*, 263109.

(6) Chang, P. C.; Fan, Z.; Chien, C. J.; Stichtenoth, D.; Ronning, C.; Liu, J. G. *Appl. Phys. Lett.* **2006**, *89*, 133113.

(7) Park, W. L.; Kim, J. S.; Yi, G. C.; Bae, M. H.; Lee, H. J. *Appl. Phys. Lett.* **2004**, *85*, 5052.

(8) Jhu, S.; Lee, K.; Yoon, M. H.; Faccheti, A.; Marks, T. J.; Janes, D. B. *Nanotechnology* **2007**, *18*, 155201.

(9) Keem, K.; Kang, J.; Yoon, C.; Jeong, D. Y.; Moon, B. M.; Kim, S. *Jpn. J. Appl. Phys.* **2007**, *46*, 6230.

(10) Xiang, B.; Wang, P.; Zhang, X.; Dayeh, S. A.; Aplin, D. P. R; Soci, C.; Yu, D.; Wang, D. *Nano Lett.* **2007**, *7*, 323.

(11) Yuan, G. D.; Zhang, W. J.; Jie, J. S.; Fan, X.; Zapien, J. A.; Leung, Y. H.; Luo, L. B.; Wang, P. F.; Lee, C. S.; Lee, S. T. *Nano Lett.* **2008**, *8*, 2591.

(12) Lu, M. P.; Song, J.; Lu, M. Y.; Chen, M. T.; Gao, Y.; Chen, L. J.; Wang, Z. L. *Nano Lett.* **2009**, *9*, 1223.

(13) Yu, W. J.; Kim, U. J.; Kang, B. R.; Lee, I. H.; Lee, E. H.; Lee, Y. H. *Nano Lett.* **2009**, *9*, 1401.

(14) Ben Jamaa, M. H.; Mohanram, K.; De Micheli, G. *Proc. Design Automation and Test in Europe* **2009**, 622−627.

(15) (a) Mensah, S. L.; Kayastha, V. K.; Ivanov, I. N.; Geohegan, D. B.; Yap, Y. K. *Appl. Phys. Lett.* **2007**, *90*, 113108. (b) Mensah, S. L.; Kayastha, V. K.; Yap, Y. K. *J. Phys. Chem. C* **2007**, *111*, 16092.

(16) McCluskey, M. D.; Jokela, S. J. *J. Appl. Phys.* **2009**, *106*, 071101.

(17) Vanheusden, K.; Warren, W. L.; Seager, C. H.; Tallant, D. R.; Voigt, J. A.; Gnade, B. E. *J. Appl. Phys.* **1996**, *79*, 7983.

(18) Ha, B. C.; Ham, H.; Lee, C. J. *J. Phys. Chem. Solids* **2008**, *69*, 2453.

(19) McCluskey, M. D.; Jokela, S. J.; Zhuravlev, K. K.; Simpson, P. J.; Lynn, K. G. *Appl. Phys. Lett.* **2002**, *81*, 3807.

(20) Damen, T. C.; Porto, S. P. S; Tell, B. *Phys. Rev.* **1966**, *142*, 570.

(21) Wang, R. P.; Xu, G.; Jin, P. *Phys. Rev. B* **2004**, *69*, 113303.

(22) Windisch, C. F.; Exarhos, G. J.; Yao, C.; Wang, L. Q. *J. Appl. Phys.* **2007**, *101*, 123711.

(23) Goldberger, J.; Sirbuly, D. J.; Law, M.; Yang, P. *J. Phys. Chem. B* **2005**, *109*, 9.

(24) Dayeh, S. A.; Aplin, D. P. R; Zhou, X.; Yu, P. K. L.; Yu, E. T.; Wang, D. *Small* **2007**, *3*, 326.

(25) Kohan, A. F.; Ceder, G.; Morgan, D.; Van de Walle, C. G. *Phy. Rev. B* **2000**, *61*, 15019.

(26) Reynolds, D. C.; Look, D. C.; Jogai, B.; Morkoc, H. *Solid State Commun.* **1997**, *101*, 643.

(27) Janotti, A.; Walle, C. G. *Rep. Prog. Phys.* **2009**, *72*, 126501.

(28) Karazhanov, S. Z.; Marstein, E. S.; Holt, A. *J. Appl. Phys.* **2009**, *105*, 033712.

(29) Lavrov, E. V.; Weber, J.; Bornert, F.; Van De Walle, C. G.; Helbig, R. *Phys. Rev. B* **2002**, *66*, 165205.

(30) Sekiguchi, T.; Ohashi, N.; Terada, Y. *Jpn. J. Appl. Phys.* **1997**, *36*, L289.

(31) Bera, A.; Basak, D. *Appl. Phys. Lett.* **2009**, *94*, 163119.

(32) Dev, A.; Niepelt, R.; Richters, J. P.; Ronning, C.; Voss, T. *Nanotechnology* **2010**, *21*, 065709.